RAA 2019 Vol. **19** No. **3**, 40(8pp) doi: 10.1088/1674–4527/19/3/40

http://www.raa-journal.org *http://iopscience.iop.org/raa*

***R**esearch in*
***A**stronomy and*
***A**strophysics*

Gas infall in the massive star formation core G192.16–3.84

Meng-Yao Tang[1], Sheng-Li Qin[1], Tie Liu[2,3] and Yue-Fang Wu[4]

[1] Department of Astronomy, Yunnan University, and Key Laboratory of Astroparticle Physics of Yunnan Province, Kunming 650091, China; *mengyao_tang@yeah.net, slqin@bao.ac.cn*

[2] Korea Astronomy and Space Science Institute, 776 Daedeokdaero, Yuseong-gu, Daejeon 34055, Republic of Korea; *liu@kasi.re.kr*

[3] East Asian Observatory, 660 N. A'ohoku Place, Hilo, HI 96720, USA

[4] Department of Astronomy, Peking University, Beijing 100871, China; *ywu@pku.edu.cn*

Received 2018 June 7; accepted 2018 October 3

Abstract Previous observations have revealed an accretion disk and outflow motion in the high-mass star-forming region G192.16–3.84, but collapse has not been reported before. Here we present molecular line and continuum observations toward the massive core G192.16–3.84 with the Submillimeter Array. $C^{18}O$(2–1) and HCO^+(3–2) lines show pronounced blue profiles, indicating gas infalling in this region. This is the first time that infall motion has been reported in the G192.16–3.84 core. Two-layer model fitting gives infall velocities of 2.0±0.2 and 2.8±0.1 km s^{-1}. Assuming that the cloud core follows a power-law density profile ($\rho \propto r^{1.5}$), the corresponding mass infall rates are (4.7±1.7)×10^{-3} and (6.6±2.1)×10^{-3} $M_\odot$ yr^{-1} for $C^{18}O$(2–1) and HCO^+(3–2), respectively. The derived infall rates are in agreement with the turbulent core model and those in other high-mass star-forming regions, suggesting that high accretion rate is a general requirement for forming a massive star.

Key words: ISM: individual objects (G192.16–3.84) — ISM: molecules — stars: formation

1 INTRODUCTION

Current observational evidence suggests that low-mass star formation typically starts with a collapsing core inside a molecular cloud. Then, the protostellar objects increase their mass by gas accretion. This process is also accompanied by outflows and an accretion disk. Collapse, accretion disk and outflow, therefore, are key elements in low mass star formation. However, the physical conditions and dynamical processes of high-mass star formation are still not well understood, due to observational difficulties caused by their short lifetimes and large distances. Outflows are often found in high-mass star-forming regions (Wu et al. 2004; Qin et al. 2008; Qiu et al. 2012). Only a handful of disks in high-mass young stellar objects, however, have been detected (Zhang et al. 1998; Shepherd et al. 2001; Jiang et al. 2005; Patel et al. 2005; Sridharan et al. 2005; Sánchez-Monge et al. 2014).

G192.16–3.84 (hereafter G192.16) is a massive protostellar system located at a distance of 1.52±0.08 kpc (Shiozaki et al. 2011). The luminosity of $\sim 3 \times 10^3\, L_\odot$ implies the presence of an early B star with a mass of 8 to 10 $M_\odot$ in this region (Shepherd & Churchwell 1996; Shepherd et al. 1998). Rich H_2O masers (Shepherd et al. 2004; Imai et al. 2006; Shiozaki et al. 2011), UC H_{II} region (Hughes & MacLeod 1993; Shepherd & Kurtz 1999), bipolar CO outflows (Shepherd et al. 1998; Liu et al. 2013a), rotational motions (Liu et al. 2013a) and a solar system-sized accretion disk (Shepherd et al. 2001) have been observed in the G192.16 region, suggesting that a massive star is forming in this region. However, collapse of the G192.16 core has not been reported before.

In this paper, we present Submillimeter Array (SMA)[1] observations of 230, 265 and 345 GHz band data towards G192.16, showing collapsing motions in this region.

[1] The SMA is a joint project between the Smithsonian Astrophysical Observatory and the Academia Sinica Institute of Astronomy and Astrophysics and is funded by the Smithsonian Institution and Academia Sinica.

2 DATA

All observational data used in our work are taken from the SMA archive. The 230, 265 and 345 GHz observations were performed with the SMA in August 2005, December 2006 and December 2011, respectively. The 230 GHz data cover CO(2–1), ^{13}CO (2–1), C^{18}O(2–1) and SO(6_5–5_4) lines with a uniform spectral resolution of 0.8125 MHz. HCO$^+$(3–2) and HCN(3–2) transitions were observed in the 265 GHz band with hybrid high-spectral resolution. The 265 GHz data have different spectral resolutions in different windows. We re-sample the 265 GHz band data to a uniform resolution of 0.8125 MHz. The 345 GHz data have a spectral resolution of 0.8125 MHz and include CO(3–2) and SO(8_8–7_7) lines. Other observational information, such as phase tracking center, bandpass calibrators, gain calibrators and flux calibrators, is listed in Table 1. Data reduction and imaging were conducted with MIRIAD (Sault et al. 1995). The continuum images were generated from line free channels. Self-calibration of the continuum data was performed to remove residual errors, and then the gain solutions were applied to line data. Synthesized beam sizes of the continuum are summarized in Table 1.

3 RESULTS

3.1 Continuum

Figure 1 presents the continuum flux density maps in both color-scale and contours. From Figure 1, one can see that the continuum images at the three wavebands show compact source structure and are unresolved.

Two dimensional (2D) Gaussian fitting was applied to the compact core. The peak position of the continuum is R.A.(J2000) = $5^{\rm h}58^{\rm m}13.547^{\rm s}$, Decl.(J2000) = $16^\circ31'58.206''$, which is consistent with that of previous continuum observations and the UC H$_{\rm II}$ region (Shepherd et al. 1998; Shepherd & Kurtz 1999; Shepherd et al. 2001; Shiozaki et al. 2011; Liu et al. 2013a). The deconvolved size, peak flux density and total flux from the Gaussian fitting are given in Table 2.

The continuum at our observed wavebands contains free-free emission ($S_\nu \propto \nu^{-0.1}$). Based on measured total flux of 1.5 mJy at the 3.6 cm band (Shepherd & Kurtz 1999), we estimate that the free-free continuum emissions are 1.07 and 1.03 mJy at the 230 and 345 GHz bands, respectively. Comparing with the total flux of the continuum at 230 and 345 GHz (0.270 to 0.769 Jy), the free-free continuum emission is negligible.

To derive physical parameters, we performed spectral energy distribution (SED) fitting based on the data from our observations and previous data at different wavelengths (Beuther et al. 2002; Shepherd et al. 1998, 2001; Williams et al. 2004). Figure 2 shows a plot of the SED. The best SED fitting gives a dust temperature $T_{\rm d}$ of 71.7±0.4 K, an H$_2$ gas column density $N_{\rm H_2}$ of $(2.7\pm1.2)\times10^{24}$ cm^{-2} and a dust emissivity index (β) of 1.7±0.4. Derived dust temperature $T_{\rm d}$ = 71.7±0.4 K is consistent with the SO$_2$ rotational temperature $T_{\rm rot}^{\rm SO_2} \sim 84^{+18}_{-15}$ K reported by Liu et al. (2013a), indicating that gas is coupled well with dust.

Gas mass of the G192.16 continuum core can be calculated by using the following formula

$$M_{\rm H_2} = \pi R^2 \cdot m_{\rm H} \cdot \mu \cdot N_{\rm H_2} \ , \qquad (1)$$

where $\mu = 2.8$ is the mean molecular weight (Kauffmann et al. 2008) and $m_{\rm H}$ is the mass of an H atom. $R = \sqrt{ab}D$ is the source size, and the major and minor axes (a and b respectively) are obtained from 2D Gaussian fitting toward the continuum core (as listed in Table 2). Note that we take major and minor axes (a and b) as 1.3″ and 0.7″ respectively, which are averaged values of the 2D Gaussian fitting results of all continuum sources. At a distance of 1.52 kpc, the core radius is calculated as $R = 0.007$ pc. Core mass ($M_{\rm H_2}$) is derived to be $10.8 \pm 4.8\ M_\odot$, which is consistent with the mass range of $4\ M_\odot \leq M_{\rm gas} + M_{\rm dust} \leq 18\ M_\odot$ estimated by Shiozaki et al. (2011).

3.2 Molecular Lines

Molecular transitions of CO(3–2), CO(2–1), ^{13}CO(2–1), C^{18}O(2–1), HCN(3–2), HCO$^+$(3–2), SO(8_8–7_7) and SO(6_5–5_4) are detected as shown in Figure 3. In Figure 3, the CO(3–2), CO(2–1), ^{13}CO(2–1), C^{18}O(2–1), HCN(3–2) and HCO$^+$(3–2) spectra display double-peaked line profiles with absorption dips at around ∼6 km s^{-1}, and the blueshifted peaks are stronger than the redshifted ones. The SO(8_8–7_7) and SO(6_5–5_4) lines show single peak profiles with local standard of rest (LSR) velocities at ∼6 km s^{-1}. These double-peaked spectral profiles are so-called "blue profiles" (Zhou et al. 1993; Wu & Evans 2003; Wu et al. 2007), indicating gas infall in this region.

Various molecular tracers (CO, CN, HCN, H$_2$CO, HCO$^+$, etc.) are used for identifying collapse candidates and studying infall (Fuller et al. 2002; Zapata et al. 2008; Wu et al. 2009, 2014; Liu et al. 2011b,a, 2013c,b; Pineda et al. 2012; Qin et al. 2016; Qiu et al. 2012). Simulations by Smith et al. (2012, 2013) suggested that HCN(3–2) and HCO$^+$(3–2) are best for studying gas infall.

From Figure 3, the CO(3–2), CO(2–1), ^{13}CO(2–1) and HCN(3–2) lines reveal much wider line wings, and these line wings may be produced by outflow motions

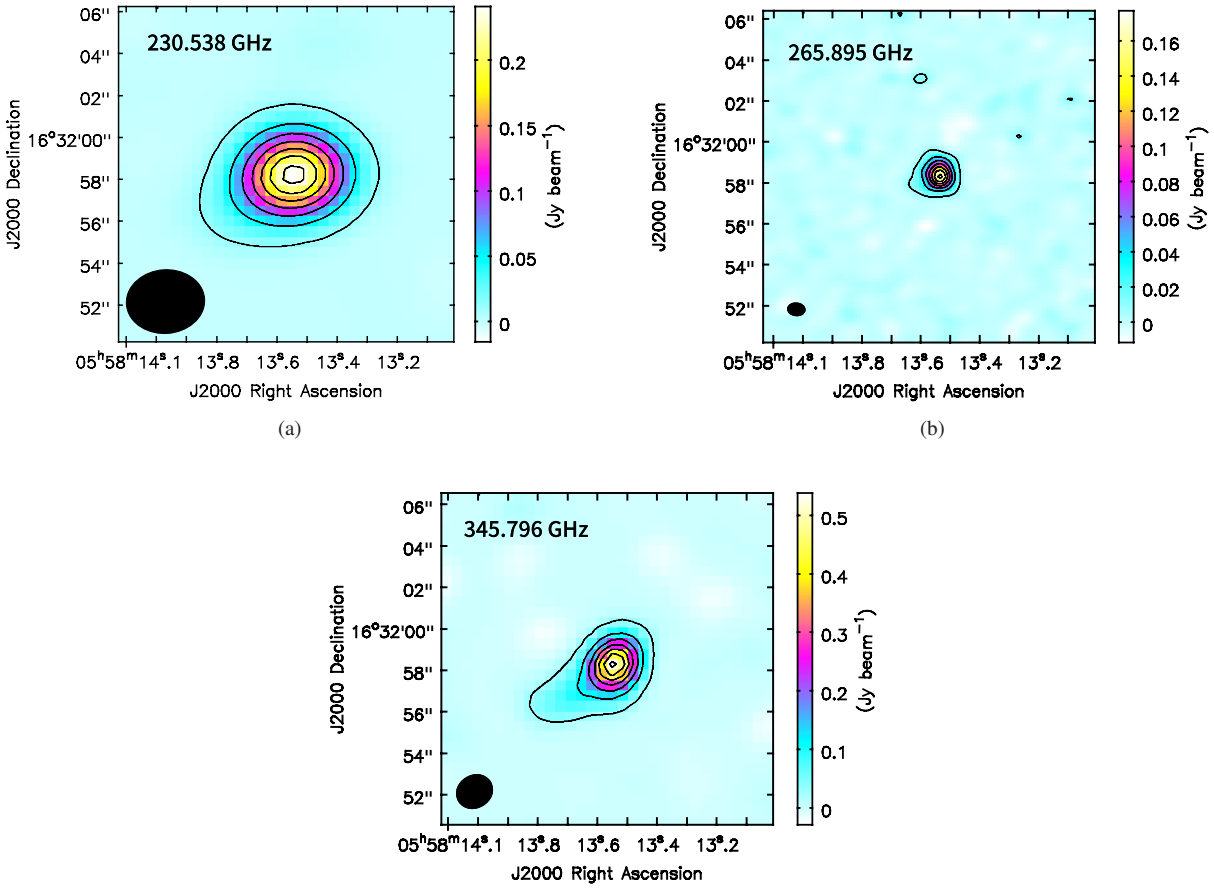

Fig. 1 Panels (a), (b) and (c) present continuum images of 230.538, 265.895 and 345.896 GHz, respectively. For all panels, the contours are from 5% to 95% of peak values (peak values are shown in Table 2), with a step of 15%. The synthesized beam size is shown in the bottom-left corner of each panel.

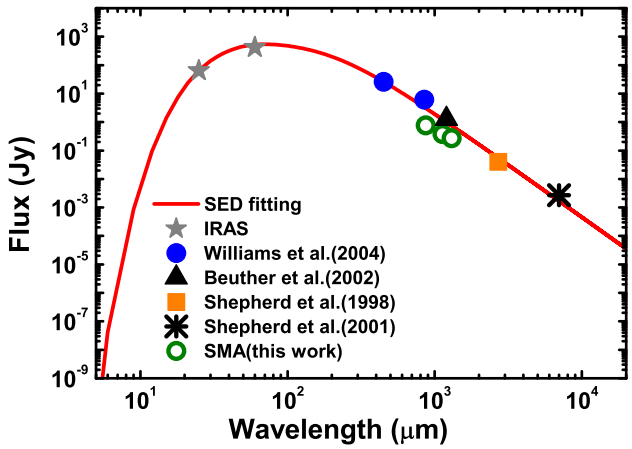

Fig. 2 SED fitting obtained from our SMA images complemented with literature and archival data at wavelengths ranging from 25 μm to 7 mm. The *red line* represents the best SED fitting. The data points are shown as *gray stars* (*IRAS*: 25 μm and 60 μm), *blue dots* (Williams et al. 2004), *black triangle* (Beuther et al. 2002), *orange square* (Shepherd et al. 1998), *black asterisk* (Shepherd et al. 2001) and *green open circles* (this work).

Table 1 SMA Observations

Phase Tracking Center (R.A, Decl.)	Band (GHz)	$N_{\rm ant}^{a}$	Calibrator			Beam Size
			Bandpass	Gain	Flux	
($5^{\rm h}58^{\rm m}13.899^{\rm s}$, $16^\circ31'59.997''$)	230	8	3C 454.3	0530+135,0510+180	Uranus	$3.74''\times3.04''(-86^\circ)$
($5^{\rm h}58^{\rm m}13.530^{\rm s}$, $16^\circ31'58.300''$)	265	8	3C 273	0528+134,0507+179	Titan	$0.86''\times0.86''(85^\circ)$
($5^{\rm h}58^{\rm m}13.549^{\rm s}$, $16^\circ31'58.300''$)	345	8	3C 84, Uranus	0530+135,0730–116	Titan	$1.80''\times1.59''(-58^\circ)$

Notes: ^{a} Number of antennas.

Table 2 Parameters of Continuum Images

Frequency (GHz)	Deconvolved Size	Peak Flux Density (Jy beam^{-1})	Total Flux (Jy)	RMS (Jy beam^{-1})
230.538	$1.5''\times0.7''(121^\circ)$	0.239±0.003	0.270±0.003	0.001
265.895	$0.9''\times0.6''(179^\circ)$	0.170±0.004	0.377±0.008	0.002
345.796	$1.6''\times0.8''(146^\circ)$	0.511±0.017	0.769±0.029	0.004

(Shepherd et al. 1998; Liu et al. 2013a). Therefore, the infall "profile" of these lines will be contaminated by outflows. $C^{18}O$(2–1) and HCO^+(3–2) lines without obvious line wings will be used for further analyses. Note that observations of $C^{18}O$(2–1) and HCO^+(3–2) lines have different angular resolutions. We have smoothed higher resolution data (HCO^+) to lower ones ($C^{18}O$).

The integrated intensity maps of $C^{18}O$(2–1) and HCO^+(3–2) are presented in Figure 4. The red cross in each panel represents the continuum emission peak. From the $C^{18}O$(2–1) map, one can see that the gas emission peak is associated with the continuum peak position. However, the HCO^+(3–2) gas is separated into two components, and one of them is also associated with the continuum peak position.

For a collapsing cloud, in case the brightness temperature of the background continuum is brighter than the excitation temperature of a "blue profile" line transition tracing infall motion, the "blue profile" line will become an "inverse P Cygni" profile. The modified two-layer model (Myers et al. 1996; Di Francesco et al. 2001) can not only fit both the "blue profile" and the "inverse P Cygni" profile, but also the "red profile" and "P Cygni" profile characterizing outflows or expansion. Then the modified two-layer model (Myers et al. 1996; Di Francesco et al. 2001) is adopted to fit the spectral profiles of $C^{18}O$(2–1) and HCO^+(3–2).

Panels (a) and (b) of Figure 5 show observed spectra in black and two-layer modeling in red for $C^{18}O$(2–1) and HCO^+(3–2), respectively. The two-layer model can be simply described as follows:

$$\begin{aligned}\Delta T_{\rm B} =&(J_{\rm f}-J_{\rm cr})\left[1-e^{(-\tau_{\rm f})}\right]\\ &+(1-\Phi)(J_{\rm r}-J_{\rm b})\left[1-e^{(-\tau_{\rm r}-\tau_{\rm f})}\right],\end{aligned} \tag{2}$$

where

$$J_{\rm cr}=\Phi J_{\rm c}+(1-\Phi)J_{\rm r}\,, \tag{3}$$

$$\tau_{\rm f}=\tau_0 e^{\left[\frac{-(V-V_{\rm in}-V_{\rm LSR})^2}{2\sigma^2}\right]}, \tag{4}$$

$$\tau_{\rm r}=\tau_0 e^{\left[\frac{-(V+V_{\rm in}-V_{\rm LSR})^2}{2\sigma^2}\right]}. \tag{5}$$

The model takes optical depth (τ_0), front layer radiation temperature ($J_{\rm f}$), rear layer radiation temperature ($J_{\rm r}$), LSR velocity ($V_{\rm LSR}$), velocity dispersion (σ), infall velocity ($V_{\rm in}$), radiation temperature of the continuum source ($J_{\rm c}$) and fill factor (Φ) into account. We adopted dust temperature $T_{\rm d}=71.7\,$K from our SED fitting as radiation temperature ($J_{\rm c}$) of the continuum source, and the fill factor (Φ) is fixed at 0.3 during the fitting process. A similar procedure was also used by Pineda et al. (2012). The $V_{\rm LSR}$ is set at $6\,{\rm km\,s^{-1}}$, which is derived from the SO(6_5–5_4) line. During the fitting process, only τ_0, $J_{\rm f}$, $J_{\rm r}$, σ and $V_{\rm in}$ are free parameters; the parameter spaces are 0.1∼10 for τ_0, 3∼100 K for $J_{\rm f}$ and $J_{\rm r}$, and $0.1\sim10\,{\rm km\,s^{-1}}$ for $V_{\rm in}$. The Levenberg-Marquardt algorithm was adopted to search for the best solution.

The best fitting gives infall velocities for the $C^{18}O$(2–1) and HCO^+(3–2) spectra of 2.0±0.2 and $2.8\pm0.1\,{\rm km\,s^{-1}}$, respectively. The detailed fitting results

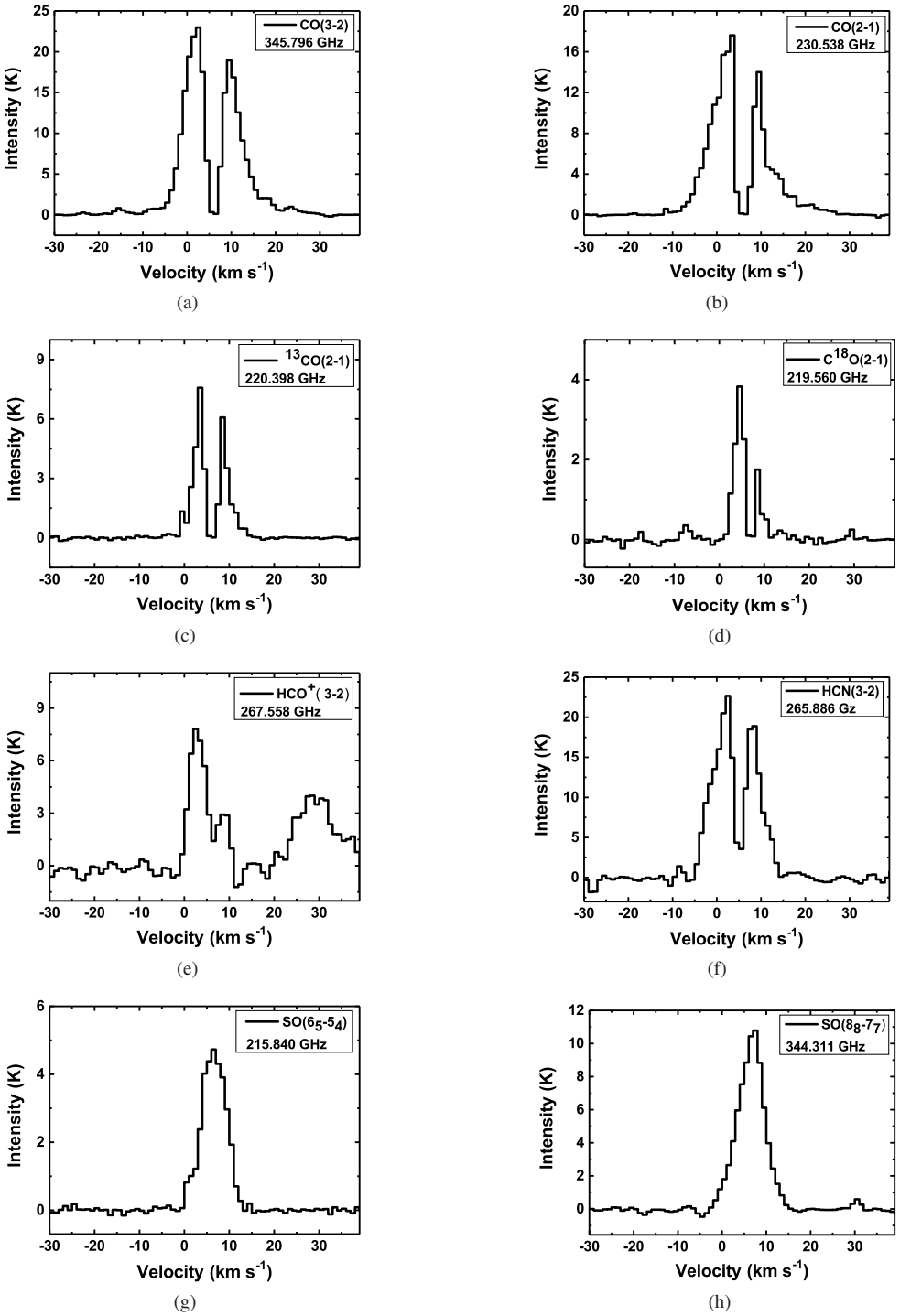

Fig. 3 All spectra are extracted from the continuum emission peak position. Line name and rest frequency are shown in the upper-right corner of each panel.

are presented in Table 3. We find that τ_0, $J_{\rm f}$ and $J_{\rm r}$ are interdependent and very sensitive to initial values. Thus, they cannot be determined accurately. In contrast, σ and $V_{\rm in}$ mainly determine the line profile. Thus, they are much less sensitive to initial values and are more reliable.

Assuming that the cloud has a power-law density profile ($\rho \propto r^{1.5}$), the mass enclosed in r_0 can be calculated by (Liu et al. 2018)

$$M = \int_0^{r_0} 4\pi r^2 \rho_0 \left(\frac{r}{r_0}\right)^{-1.5} dr \ , \qquad (6)$$

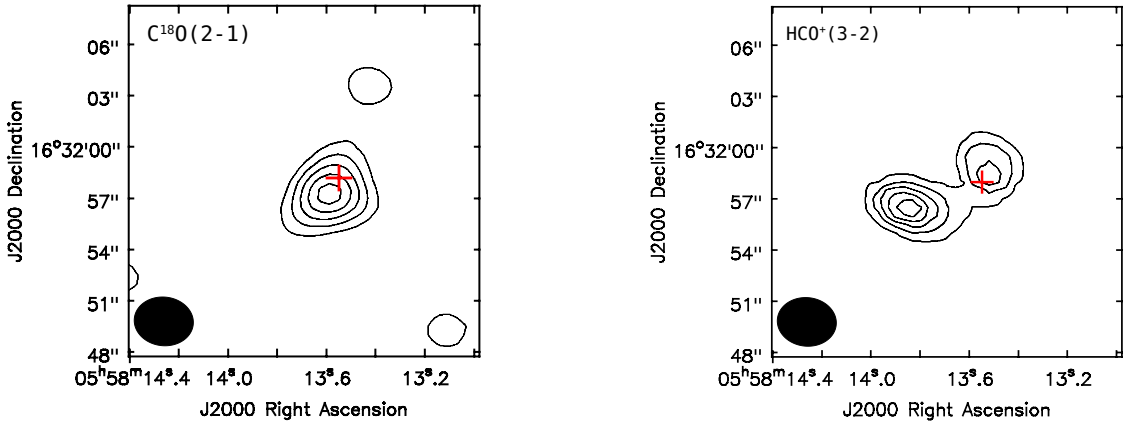

(a) (b)

Fig. 4 Panels (a) and (b) present integrated intensity maps of $C^{18}O$(2–1) and HCO^+(3–2) transitions, respectively. The *red cross* in each panel is the continuum emission peak of G192.16. The contour levels are from 10% to 90%, with step of 20%. The beam sizes of these two observations are shown in the bottom-left corner of each panel. The HCO^+(3–2) map is smoothed to the same resolution as the $C^{18}O$(2–1) map.

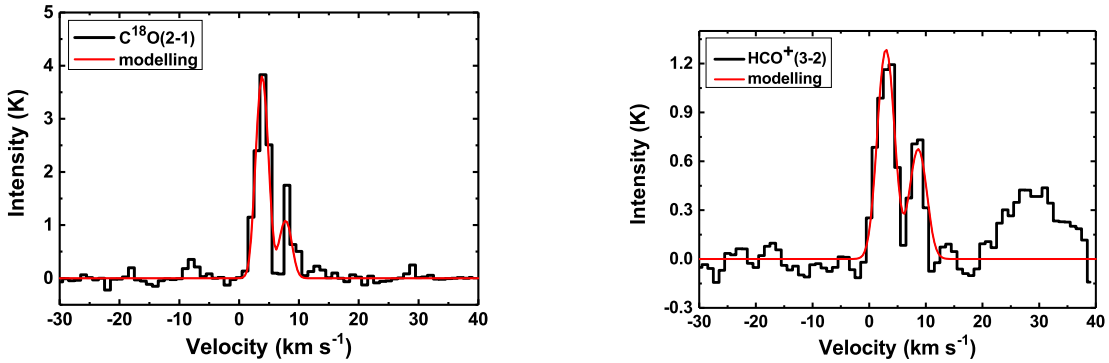

(a) (b)

Fig. 5 Panels (a) and (b) present observed lines (*black*) and two-layer modeling (*red*) of $C^{18}O$(2–1) and HCO^+(3–2), respectively. The line name is shown in the upper-left corner of each panel. The fitting results are listed in Table 3.

Table 3 Fitting Results of the Two-layer Model

Line	τ_0	J_f (K)	J_r (K)	σ (km s^{-1})	V_{in} (km s^{-1})	M_{in} ($M_\odot$ yr^{-1})
$C^{18}O$(2–1)	0.7±0.4	23.8±2.4	11.1±4.7	0.9±0.4	2.0±0.2	(4.7±1.7)×10^{-3}
HCO^+(3–2)	0.4±0.1	23.6±0.3	5.5±0.4	1.4±0.1	2.8±0.1	(6.6±2.1)×10^{-3}

Notes: Optical depth (τ_0), front layer radiation temperature (J_f), rear layer radiation temperature (J_r), velocity dispersion (σ) and infall velocity (V_{in}) are free parameters in the fitting, while infall rate (M_{in}) is calculated by using fitted infall velocity.

where r_0 is the outer radius and ρ_0 is the density at r_0. Thus, the mass infall rate can be estimated as

$$M_{in} = 4\pi r_0^2 \rho_0 V_{in} = 1.5 M V_{in}/r_0 \ . \quad (7)$$

We adopt the mass of $10.8\,M_\odot$ from the SED fitting for M and the averaged source size (R) of 0.007 pc for r_0. Thus the mass infall rates of $C^{18}O$(2–1) and HCO^+(3–2) are estimated to be (4.7±1.7)×10^{-3} and $(6.6 \pm 2.1) \times 10^{-3}\,M_\odot$ yr^{-1}, respectively. The infall rates are also summarized in Table 3.

4 DISCUSSION AND CONCLUSIONS

Rich H_2O masers (Shepherd et al. 2004; Imai et al. 2006; Shiozaki et al. 2011), UC H_{II} regions (Hughes & MacLeod 1993; Shepherd & Kurtz 1999), bipolar CO(1-0) outflows

(Shepherd et al. 1998; Liu et al. 2013a) and an accretion disk (Shepherd et al. 2001) in G192.16 have been reported by previous observations, indicating that a massive star is forming in this region.

We have identified gas infall in the G192.16 region, using $C^{18}O$(2–1) and HCO^+(3–2) lines, for the first time. The infall rates derived from these transitions are $(4.7\pm1.7)\times10^{-3}$ and $(6.6\pm2.1)\times10^{-3}\,M_\odot$ yr^{-1}, respectively. Inflow motions have been reported toward some massive star-forming regions, with mass infall rates ranging from 10^{-4} to $10^{-2}\,M_\odot$ yr^{-1} (Zhang & Ho 1997; Sandell et al. 2005; Beltrán et al. 2006; Garay et al. 2007; Zapata et al. 2008; Wu et al. 2009, 2014; Liu et al. 2011b,a, 2013c,b; Qin et al. 2016; Qiu et al. 2012). The derived infall rate toward G192.16 is consistent with those in other high-mass star formation regions.

In this work, the infall rate of $C^{18}O$(2–1) is $(4.7\pm1.7)\times10^{-3}\,M_\odot$ yr^{-1}. The HCO^+(3–2) line has higher critical density than that of $C^{18}O$(2–1) and it is generally used for tracing dense and inner parts of molecular clouds. An infall rate of $(6.6 \pm 2.1) \times 10^{-3}\,M_\odot$ yr^{-1} is derived from HCO^+(3–2), which is larger than that of $C^{18}O$(2–1). The scenario appears to indicate that infall is faster in the inner and denser region than in the outer part of the G192.16 core. This is the first time that infall motions have been reported in the massive core G192.16. The turbulent core model (McKee & Tan 2003) considers a core having density structure of $\rho \propto r^{1.5}$, and a resulting accretion rate of more than $\sim 10^{-3}\,M_\odot\,\mathrm{yr}^{-1}$ will be high enough to overcome radiation pressure to form a massive star. In our case, the derived infall rate is $\sim 5 \times 10^{-3}\,M_\odot$ yr^{-1} by assuming that the dense core has a power-law density profile ($\rho \propto r^{1.5}$). The infall rates of our fitting are consistent with the predictions of McKee & Tan (2003). Recent numerical simulations have shown that massive stars are formed by disk accretion and the radiation pressure barrier can be easily overcome when an optically thick accretion disk is taken into account (Kuiper et al. 2010; Kuiper & Yorke 2013). An accretion disk was also reported in G192.16. All this evidence indicates that a massive star is forming in the G192.16 core by gas accretion, and high accretion rate is a general requirement for the formation of a massive star.

Acknowledgements This work has been supported by the National Key R&D Program of China (No. 2017YFA0402701) and by the National Natural Science Foundation of China (Grant Nos. 11373026 and 11433004), and the Joint Research Fund in Astronomy (U1631237) under cooperative agreement between the National Natural Science Foundation of China and Chinese Academy of Sciences, and by the Top Talents Program of Yunnan Province (2015HA030), and by Yunnan University's Research Innovation Fund for Graduate Students.

References

Beltrán, M. T., Cesaroni, R., Codella, C., et al. 2006, Nature, 443, 427
Beuther, H., Schilke, P., Menten, K. M., et al. 2002, ApJ, 566, 945
Di Francesco, J., Myers, P. C., Wilner, D. J., Ohashi, N., & Mardones, D. 2001, ApJ, 562, 770
Fuller, G. A., Williams, S. J., & Sridharan, T. K. 2002, in Bulletin of the American Astronomical Society, 34, American Astronomical Society Meeting Abstracts #200, 762
Garay, G., Mardones, D., Bronfman, L., et al. 2007, A&A, 463, 217
Hughes, V. A., & MacLeod, G. C. 1993, AJ, 105, 1495
Imai, H., Omodaka, T., Hirota, T., et al. 2006, PASJ, 58, 883
Jiang, Z., Tamura, M., Fukagawa, M., et al. 2005, Nature, 437, 112
Kauffmann, J., Bertoldi, F., Bourke, T. L., Evans, II, N. J., & Lee, C. W. 2008, A&A, 487, 993
Kuiper, R., Klahr, H., Beuther, H., & Henning, T. 2010, ApJ, 722, 1556
Kuiper, R., & Yorke, H. W. 2013, ApJ, 763, 104
Liu, H. B., Qiu, K., Zhang, Q., Girart, J. M., & Ho, P. T. P. 2013a, ApJ, 771, 71
Liu, T., Wu, Y., Liu, S.-Y., et al. 2011a, ApJ, 730, 102
Liu, T., Wu, Y., Wu, J., Qin, S.-L., & Zhang, H. 2013b, MNRAS, 436, 1335
Liu, T., Wu, Y., & Zhang, H. 2013c, ApJ, 776, 29
Liu, T., Wu, Y., Zhang, Q., et al. 2011b, ApJ, 728, 91
Liu, T., Li, P. S., Juvela, M., et al. 2018, ApJ, 859, 151
McKee, C. F., & Tan, J. C. 2003, ApJ, 585, 850
Myers, P. C., Mardones, D., Tafalla, M., Williams, J. P., & Wilner, D. J. 1996, ApJ, 465, L133
Patel, N. A., Curiel, S., Sridharan, T. K., et al. 2005, Nature, 437, 109
Pineda, J. E., Maury, A. J., Fuller, G. A., et al. 2012, A&A, 544, L7
Qin, S.-L., Wang, J.-J., Zhao, G., Miller, M., & Zhao, J.-H. 2008, A&A, 484, 361
Qin, S.-L., Schilke, P., Wu, J., et al. 2016, MNRAS, 456, 2681
Qiu, K., Zhang, Q., Beuther, H., & Fallscheer, C. 2012, ApJ, 756, 170
Sánchez-Monge, Á., Beltrán, M. T., Cesaroni, R., et al. 2014, A&A, 569, A11
Sandell, G., Goss, W. M., & Wright, M. 2005, ApJ, 621, 839
Sault, R. J., Teuben, P. J., & Wright, M. C. H. 1995, in Astronomical Society of the Pacific Conference Series, 77,

Astronomical Data Analysis Software and Systems IV, eds. R. A. Shaw, H. E. Payne, & J. J. E. Hayes, 433
Shepherd, D. S., & Churchwell, E. 1996, ApJ, 472, 225
Shepherd, D. S., Watson, A. M., Sargent, A. I., & Churchwell, E. 1998, ApJ, 507, 861
Shepherd, D. S., & Kurtz, S. E. 1999, ApJ, 523, 690
Shepherd, D. S., Claussen, M. J., & Kurtz, S. E. 2001, Science, 292, 1513
Shepherd, D. S., Borders, T., Claussen, M., Shirley, Y., & Kurtz, S. 2004, ApJ, 614, 211
Shiozaki, S., Imai, H., Tafoya, D., et al. 2011, PASJ, 63, 1219
Smith, R. J., Shetty, R., Stutz, A. M., & Klessen, R. S. 2012, ApJ, 750, 64
Smith, R. J., Shetty, R., Beuther, H., Klessen, R. S., & Bonnell, I. A. 2013, ApJ, 771, 24
Sridharan, T. K., Williams, S. J., & Fuller, G. A. 2005, ApJ, 631, L73
Williams, S. J., Fuller, G. A., & Sridharan, T. K. 2004, A&A, 417, 115
Wu, J., & Evans, II, N. J. 2003, ApJ, 592, L79
Wu, Y., Wei, Y., Zhao, M., et al. 2004, A&A, 426, 503
Wu, Y., Henkel, C., Xue, R., Guan, X., & Miller, M. 2007, ApJ, 669, L37
Wu, Y., Qin, S.-L., Guan, X., et al. 2009, ApJ, 697, L116
Wu, Y., Liu, T., & Qin, S.-L. 2014, ApJ, 791, 123
Zapata, L. A., Palau, A., Ho, P. T. P., et al. 2008, A&A, 479, L25
Zhang, Q., & Ho, P. T. P. 1997, ApJ, 488, 241
Zhang, Q., Hunter, T. R., & Sridharan, T. K. 1998, ApJ, 505, L151
Zhou, S., Evans, II, N. J., Koempe, C., & Walmsley, C. M. 1993, ApJ, 404, 232